ChemistrySelect

Research Article
doi.org/10.1002/slct.202202820

Chemistry Europe
European Chemical
Societies Publishing

www.chemistryselect.org

Plasma Spraying of Kaolinite for Preparing Reactive Alumino-Silicate Glass Coatings

Laurence N. Warr,*[a] Thorben Wolff,*[b] Holger Testrich,*[b] Georg Grathoff,[a] Angela Kruth,[b] and Rüdiger Foest[b]

Thermally treated kaolinite is used to develop a range of alumino-silicate-based precursor materials but its behavior during plasma spraying has not been well-researched. In this study, two types of kaolinite samples were investigated in the form of low defect (KGa-1b) and high defect (KGa-2) varieties. The extreme temperatures of the plasma stream (up to 20 000 K) induced flash melting to produce a highly porous alumino-silicate glass without any crystallization of new Al–Si oxide minerals. The glass is comprised largely of intact or deformed spheres (average diameters 1.14–1.44 μm), which indicates rapid quenching and solidification before impact. The subspherical structures contain up to 40 % closed pore space caused by the rapid escape of water during melting. The low-density, porous alumino-silicate glass coatings with predicted specific surface areas (>0.95 m^2/g) and hardnesses >1.8 GPa represent a potentially reactive but physically stable substrate ideal for further chemical functionalization.

Introduction

Preparing reactive substrates represents an important initial step in chemically engineering the surface properties used to develop a range of advanced materials.[1–3] In addition to organically modified substrates, inorganic mineral coatings offer diverse physical-chemical properties that can be functionalized to perform specific tasks. These are particularly relevant to a broad range of technical and environmental applications,[4] and lie at the forefront of tackling problems such as those linked to CO_2 capture, pollution control, the safe storage of radioactive waste and developing advanced space applications.[5–8]

The most studied mineral for developing alumino-silicate-based substrates is kaolinite ($Al_2Si_2O_5OH_4$). This sheet silicate mineral is held together by distinct hydroxyl layers that when thermally treated between 723 and 973 K (450 and 700 °C) loses its OH$^-$ groups as structural water. This leads to highly reactive 5-fold Al clusters arranged in a disordered X-ray amorphous material known as metakaolinite.[9,10] Such thermally treated precursor minerals are used to develop new materials ranging from alkali-activated geopolymer cements to ceramic insulators.[11,12] At higher temperatures, kaolinite is known to produce increasingly amorphous phases and at 1173 K ($>$ 900 °C) crystallizes to form spinel, mullite and cristobalite;[13] a step known to significantly reduce the reactivity of the Al–Si precursor material.[14] Thermal analyses show kaolinite dehydroxylation to be strongly dependent on the heating rate whereby flash heating at high temperatures leads to retarded OH$^-$ loss and vesicle formation compared to prolonged heating at lower temperatures.[15]

Although the solid-state thermal transformation of kaolinite to dehydroxylated metakaolinite is well-constrained, the transition into a melt phase has not been extensively researched. In its pure form, kaolinite has a high melting point at 1 bar of 2123 K,[16] whereas, at higher pressure conditions, molecular calculations indicate melting to a liquid condition to occur at 1818 K at 8.85 GPa.[17] One novel approach to studying the incongruent melting process is to use atmospheric plasma spraying (APS). The high-temperature conditions of the plasma (up to 20 000 K) cause the material to rapidly dehydroxylate and melt. The high velocity of the plasma jet accelerates the material towards a substrate where it is quenched and solidifies to form a thin coating. Its deposition rate is in the order of kilograms per hour and the particle diameters typically fall in the range of a few to some hundred micrometers in diameter. This process has been used to develop a wide range of materials such as metals, ceramics and composites.[18] The plasma coatings result in surfaces with improved resistance to physical wear, chemical corrosion and may act as thermal barriers or develop biocompatible properties.[19–25] Plasma coatings of mullite, for example, are considered to have suitable properties for the thermal and radiation protection of space launch vehicles.[26,27] A related method to plasma spraying is the in situ plasma magmavication of kaolin soils to produce vitrified rock, which has been tested as a remediation method for retaining pollutants.[28]

To our knowledge, only one study has been conducted on the plasma spraying of kaolinite. Nevrla et al.[29] sprayed a kaolin sample with 75 % kaolinite abundance using a water-stabilized plasma torch. In their proof-of-concept study, they

[a] *Prof. Dr. L. N. Warr, Dr. G. Grathoff*
Institute of Geography and Geology, University of Greifswald, D-17487 Greifswald, Germany
E-mail: warr@uni-greifswald.de
[b] *Dr. T. Wolff, Dr. H. Testrich, Dr. A. Kruth, Dr. R. Foest*
Leibniz Institute for Plasma Science and Technology (INP), Felix-Hausdorff-Str. 2, 17489 Greifswald, Germany
E-mail: thorben.wolff.physik@gmail.com
holger.testrich@inp-greifswald.de

ChemistrySelect

Research Article
doi.org/10.1002/slct.202202820

Chemistry Europe

European Chemical
Societies Publishing

demonstrated that low-density amorphous metakaolinite coatings could be prepared using this method but did not document the reaction or material in detail. In the present study, we investigate the mechanisms of kaolinite melting by APS using two well-studied standard samples (KGa-1b and KGa-2) that are taken as examples of this sheet silicate mineral with different densities of crystal defects. Our primary aim was i) to study the nature of melt formation that occurred under plasma conditions, ii) to establish any dependence on the differences in the kaolinite crystal structure, and iii) to determine the optimal conditions for plasma spraying. Based on our analyses by X-ray diffraction (XRD), focused-ion-beam scanning electron microscopy (FIB-SEM), transmission electron microscope (TEM) and attenuated total reflection Fourier-transform infrared absorption microscopy (ATR FT-IR), we demonstrate how APS can be used to prepare potentially highly reactive but physically stable, low density and porous aluminosilicate glass coatings with properties suitable for further chemical functionalization.

Experimental section

Kaolinite samples

Low-defect (KGa-1b) and high-defect varieties of kaolinite (KGa-2) were obtained from the Clay Minerals Society (https://www.clays.org/sourceclays_data/). These standard materials are considered typical of many naturally occurring kaolinites and have high purities approaching ca. 96%. According to Chipera and Bish,[30] both samples contain similar accessory minerals, namely 3% anatase, 1% crandallite and traces of mica or illite (Table 1). Due to the relatively high purity of kaolinite, the Al:Si ratios of the two samples powder are close to 1:1 and both show similar oxide compositions. The main difference in elemental composition between these samples is that KGa-1b contains slightly lower amounts of Fe_2O_3 than KGa-2 with 0.35 and 1.15%, respectively (Table 1).[31]

The KGa-1b kaolinite has an almost defect-free and ordered structure, whereas the disordered KGa-2 kaolinite contains numerous stacking faults that displace adjacent layers in arbitrary lengths and directions.[34] The well-crystallized nature of KGa-1b is reflected in the lower specific surface area of KGa-1b with $10.05 +/-0.02$ m^2/g as reported by van Olphen and Fripiat.[32] The disordered KGa-2 sample has a significantly higher specific surface area of $23.50 +/-0.06$ m^2/g. These authors also determined the total OH$^-$ contents to be 13.11% and 13.14%, respectively (Table 1).

Upon laboratory heating, kaolinite dehydroxylates between 450°C and 600°C whereby it transforms into metastable, X-ray amorphous, metakaolin by the following reaction:[35]

$$Al_4Si_4O_{10}(OH)_8 \rightarrow 2Al_2Si_2O_7 + 4H_2O$$
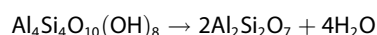
During heating, kaolinite loses its chemically bound water molecules in two steps. At first, the hydroxyl groups from the interlayers are released with an activation energy between 149 to 162 kJ mol^{-1} (Figure 1). This is followed by the release of the inner hydroxyl groups with an activation energy 87–92% of the first dehydroxylation stage.[36]

The high-defect kaolinite is reported to dehydroxylate more rapidly than the low-defect kaolinite.[38] Thermogravimetric analysis by Guggenheim and Koster van Gross[39] indicates that 12.13% of hydroxyl groups are lost during heating to 873 K (600°C) compared to the theoretical content of 14% for pure $Al_2Si_2O_5(OH_4)$. Upon further heating, melting begins at 1236 K (963°C) and is usually complete by 361 K (988°C). Al–Si spinel and amorphous silica are produced in the range of 973 K (700°C) to 1223 K (950°C).[35] When heated at temperatures above 1373 K (1100°C), 3:1 mullite ($Al_6Si_2O_{13}$) is known to crystallize as the stable phase.[40] At higher temperatures, this may be accompanied by the crystallization of cristobalite from the amorphous silica species.

Table 1. Mineral properties of the KGa-1b and KGa-2 kaolinite samples.[30–32] IMA-CNMNC approved mineral symbols; Kln = kaolinite, Ant = anatase, Cdl = crandallite, Dck = dickite, Mca = mica and Ilt = illite.[33]

Sample	Defect structure	Mineral.[30] %	Oxide	Abundance.[31] %	OH$^-$ content.[32] %	Specific surface area (N$_2$)[32] m^2/g^2
KGa-1b	Low	Kln 96	SiO$_2$	43.36	13.11	$10.05 +/-0.02$
		Ant 3	Al$_2$O$_3$	38.58		
		Cdl 1	Fe$_2$O$_3$	0.35		
		[Dck]	TiO$_2$	1.67		
			MgO	0.04		
			CaO	0.04		
			Na$_2$O	0.05		
			P$_2$O$_5$	0.0		
KGa-2	High	Kln 96	SiO$_2$	43.49	13.14	$23.50 +/-0.06$
		Ant 3	Al$_2$O$_3$	38.14		
		Cdl 1	Fe$_2$O$_3$	1.15		
		[Mca/Ilt]	TiO$_2$	1.91		
			MgO	0.04		
			CaO	0.03		
			Na$_2$O	0.06		
			K$_2$O	0.02		
			P$_2$O$_5$	0.32		
[trace amount]						

ChemistrySelect

Research Article
doi.org/10.1002/slct.202202820

Chemistry
Europe
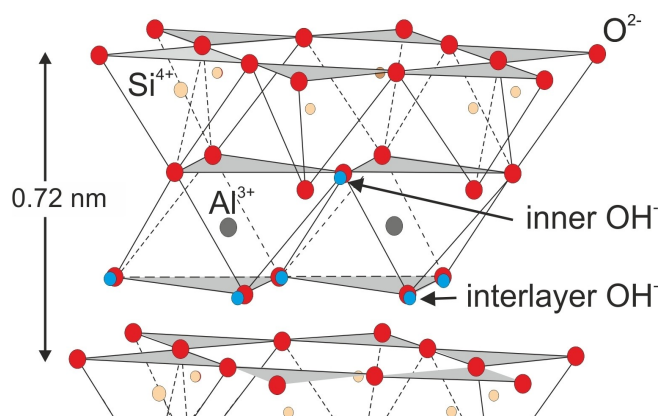European Chemical
Societies Publishing

Figure 1. Crystal structure of kaolinite showing the location of inner and interlayer OH⁻ groups that are released at different temperatures. Modified after Grim.[37]

Figure 2. Schematic representation of the experimental setup for plasma spraying kaolinite.

Experimental setup

The kaolinite powder KGa-1b has a grain size range of 700 nm to 50 μm whereas the KGa-2 falls in the size range of 650 nm to 40 μm. Both powders were heated to 313 K (40 °C) before plasma spraying to reduce any clumping and sticking of the material due to surface water.

The two kaolinite powders were used for atmospheric APS to produce thin coatings on flat metal substrates composed of Ti-6Al-4V (DOT GmbH Charles-Darwin-Ring 1a 18059 Rostock) or stainless steel (Type 1.4301: AISI 304 from Hans-Erich Gemmel & Co GmbH Bessemerstraße 76b, 12103 Berlin). The Ti-6Al-4V plates were purchased with corundum grit-blasted surfaces that were prepared by the manufacturer. The stainless steel substrates were grit-blasted in the INP laboratory using corundum powder at ca. 4 bar and ca. 10 seconds with a blasting angle of 90°. Surfaces were thoroughly cleaned with isopropanol before the coating process but without ultrasonic treatment. The flat 1 mm thick metal plates were cut into 5×5 cm format before spraying.

A F4MB-XL plasma spray torch from Oerlikon Metco was used for this study, which was mounted on an IRB-2600 robot from ABB. The sample conveyor system consisted of a modified Twin-120-A powder conveyor, a gas inlet and a flexible tube connecting the powder feeder with the plasma spray gun (Figure 2).

The process parameters for the experiments are listed in Table 2. Different specimens were prepared by varying the number of
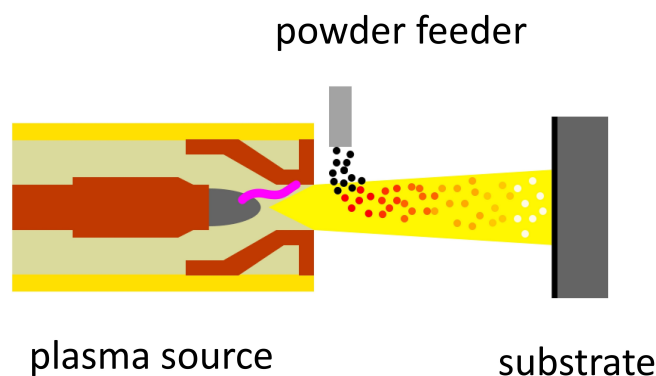
plasma passes to form a coating with one, two, or five layers. Coating speeds were either 100 or 200 mm/s with spray distances of 85 mm. One five-layer coated specimen of KGa-2 was subjected to an additional heating pass at 600 A flushed with Ar and H₂ gas. These passes were was aimed to melt the top layer and study the effects of static heating as an additional stage of treatment. The precise temperature of this treatment could not be determined.

Analytical methods

Following plasma spraying, the metal plates were studied by XRD using a theta-theta Bruker Advance D8 diffractometer equipped with a LynEye strip detector and a Co-tube (40 kV, 30 mA) and a Fe filter. The plates were mounted directly onto the diffractometer and measurements were obtained from the intact plasma sprayed coating. XRD patterns were acquired by scanning from 6° to 60° 2theta using a 0.02 step size and a variable slit scanning mode to assure that the irradiated area remained the same.

The specimens were then studied by SEM using a field emission Auriga Zeiss FIB-SEM microscope. Due to the metal substrate, the samples could be imaged without using a conductive coating. Images were obtained at 1 kV to further reduce any electron surface charging of the specimen. A range of secondary electron images was obtained at a working distance of 5 mm from different areas of the specimens at magnifications between ×100 and ×15 000. The quality of the images could resolve particles as small as 20 nm in size.

The nature of the platy particles coating the glass beads was investigated by TEM. For this study, plasma-coated specimens were

Parameter set	1	2	3	4	5	6	6
Substrate	stainless steel*	stainless steel *	Ti-6Al-4 V	Ti-6Al-4 V	Ti-6Al-4 V	Ti-6Al-4 V	Ti-6Al-4 V
Powder	KGa-1b	KGa-2	KGa-2	KGa-2	KGa-2	KGa-2	KGa-2
Coating passes	2	2	1	1	2	5	5
Additional heating	0	0	0	1	0	0	1
Pass speed (mm/s)	100	100	200	200	200	200	200
Argon (slm)	41	41	41	41	41	41	41
Hydrogen (slm)	14	14	14	14	14	14	14
Current (A)	600	600	600	600	600	600	600
Distance (mm)	75	75	75	75	75	75	75

Table 2. Process parameters for the atmospheric plasma spray depositions. *Stainless steel type 1.4301 (AISI 304).

ChemistrySelect

Research Article
doi.org/10.1002/slct.202202820

Chemistry Europe
European Chemical
Societies Publishing

placed in a small glass beaker with distilled water and the fine particles were brought into suspension using a small 35 kHz ultrasonic bath. A few drops of the strongly diluted suspension were then pipetted onto a polyvinyl formal carbon film substrate stretched over a TEM sample grid. The TEM specimens were examined using a JEOL JEM 2100PLU microscope equipped with an Oxford instruments X-max 100 mm² energy dispersive X-ray (EDX) detector. The platy nanoparticles were imaged at a magnification of ×40 000 to ×200 000 with selected area diffraction (SAED) and EDX analyses made of the same areas.

ATR FT-IR spectroscopy was performed with a Perkin Elmer, Spectrum Spotlight 200 microscope. The spectra were obtained with a spectral resolution of 4 μm in the range between 4000 and 650 cm⁻¹ through an ATR germanium crystal (L186-0268). A polynomial baseline correction was applied to all resulting transmission spectra.

Results and discussion

Phase identification by X-ray diffraction

When compared with the mineralogy of the raw materials, all XRD patterns of the plasma sprayed coating showed a close to complete transformation of the material to an X-ray amorphous state with similar features to dehydroxylated kaolinites documented in the literature (Figure 3).[40] Only a very small (001) reflection at 0.7 nm was detectable after treatment, indicating traces of kaolinite remained that did not lose complete structural ordering in the crystallographic c*-direction (Figure 3b). That most kaolinite transformed to X-ray amorphous metakaolinite is evident from the broad elevation in the background centered on 0.35 nm, which is typical of the dehydroxylated state. The second hump in the background level at around 0.18 nm was caused by the metal substrate. Other minor reflections occurring at 0.356 nm (002 of kaolinite and anatase) and 0.253 nm (crandallite) are attributed to accessory minerals present in the original sample. The distinct reflections at 0.252, 0.20, 0.161, 0.154 and 0.143 nm also result from the metal stainless steel substrate. Characteristic mullite reflections at 0.339, 0.343 and 0.221 nm were absent in all XRD patterns and no anatase or crandallite reflections could be recognized. The melting points of these three minerals are 2101, 2140 and 1528 K, respectively.[40–43]

No significant differences in the XRD patterns could be detected when comparing the number of plasma spray coatings applied. The XRD characteristics of the single plasma layered coating were essentially the same as the five-layered coating. Specimens subjected to an additional plasma heating stage also showed no distinct variation and their XRD patterns were close to identical to specimens that did not receive a secondary heat treatment.

Characterization of the plasma coatings by electron microscopy

Low magnification (×100) SEM images of all plasma coatings show a relatively homogenous distribution of porous material across the surface area of the metal substrate. At high
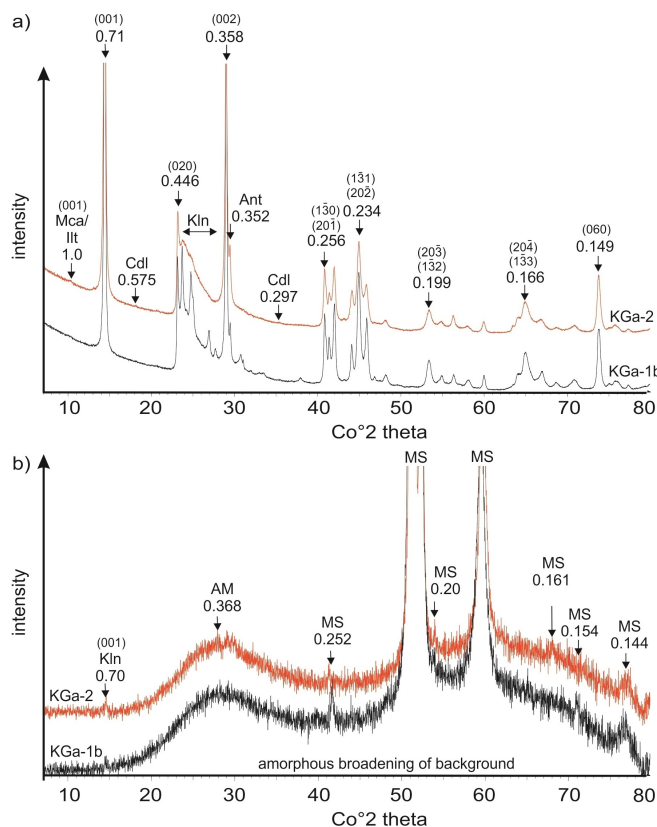

Figure 3. a) X-ray diffraction patterns of the two raw kaolinite powders investigated; KGa-1b (black) and KGa-2 (red). Miller Indices of kaolinite reflections are shown in brackets. All positions of reflections are given in nm. b) X-ray diffraction pattern of the plasma sprayed glass sphere coatings. The main reflections at 0.207, 0.232, and 0.18 nm represent the stainless steel metal substrate (MS). See Table 1 for a list of mineral symbols.

magnifications (> ×5000), small alumino-silicate spheres and ellipsoid-shaped micrometer-sized bodies are visible within the coatings along with occasional patches of some smooth sheeted material (Figure 4). As these structures show signs of flow and plastic deformation, they are considered to represent melt material that formed as viscous droplets in the plasma field and then quenched during rapid cooling as the material was deposited on the metal substrate.

Other than forming a thicker plasma coating, the five-layered film shows similar features as that observed in the single-layer coating (Figure 4c). In many coatings, there is a localized sequence in the size of the droplets from large to smaller droplets with time, which resulted in smaller spheres lying on larger ones (Figure 4b). Many of the smaller bodies were also flattened as they impacted the surface. As no impact structures were observed in the underlying material, it is suggested that much of the melt rapidly solidified during attachment to the substrate.

A FIB-SEM polished ion milled section through one of the glass beads reveals a highly porous internal structure (Figure 4d). About 40% is made up of rounded pores ranging in size from nm to μm. Many of the smaller mesopores are not connected and are considered to form as vesicles as water
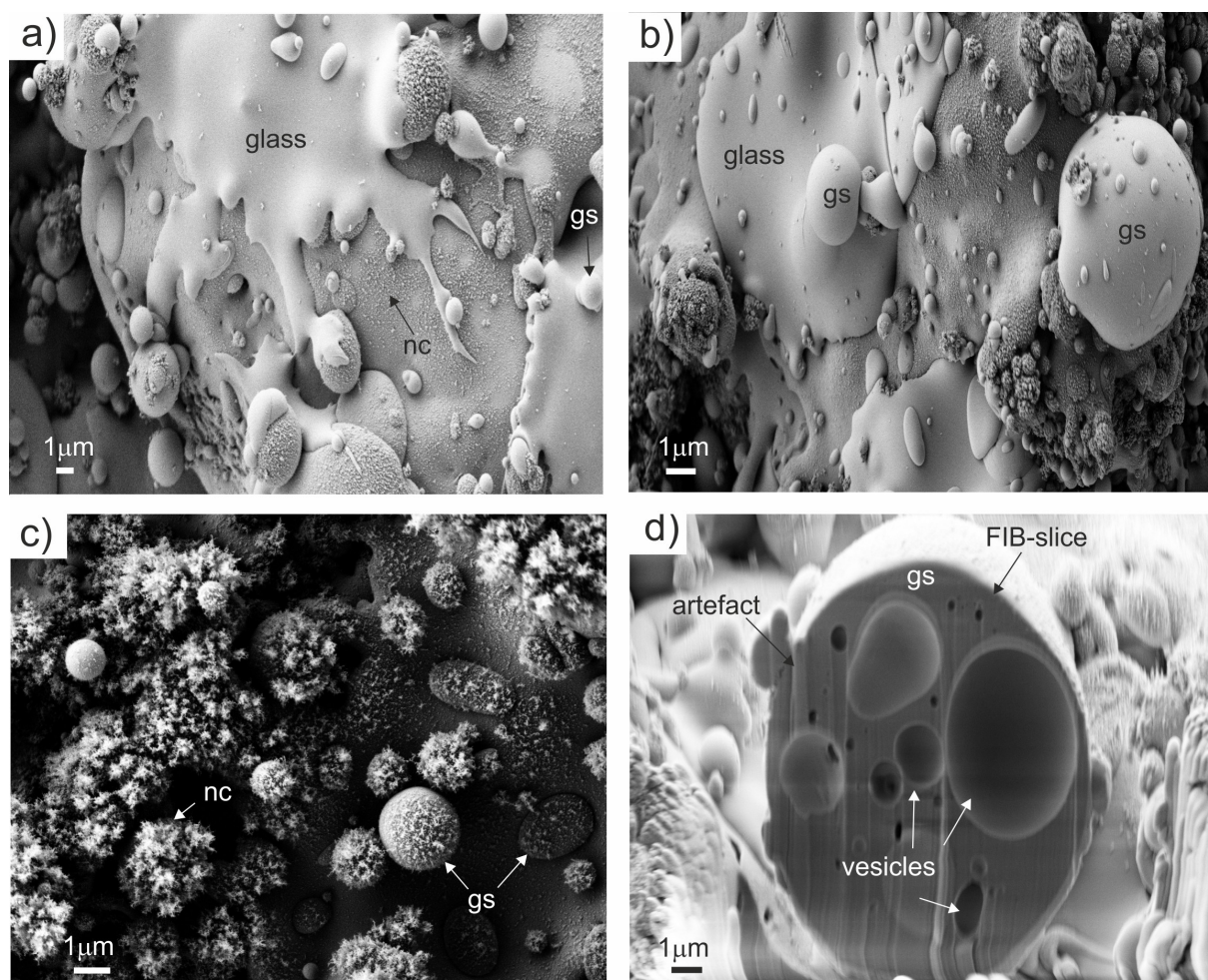
ChemistrySelect

Research Article
doi.org/10.1002/slct.202202820

Chemistry Europe
European Chemical
Societies Publishing

Figure 4. Secondary electron images of plasma-sprayed kaolinite a) single-layer coating, b) double-layer coating, c) individual glass sphere (gs) in five-layer coating and d) ion-milled focused ion beam (FIB) polished cut through a glass sphere in the five-layer coating with additional heat treatment. nc = nanocrystalline phase.

vaporized under high temperatures. Other sectioning into the surface of the films showed similarly high porosities. These features are alike to those developed in volcanic glasses in the presence of volatile gases or in the shock melting of sediment (tektite) during meteorite impacts.[44–46] The high porosity of the coatings may also be related to the very high viscosity of the alumino-silicate melt as documented in studies of thin plasma-sprayed mullite.[26,27]

A fine-grained, nanocrystalline material is seen to coat the droplet structures in all specimens (Figure 5a–d). These particles are largely platy in shape and formed small clusters that adhered to the surface of the glass spheres. They are considered to represent small amounts of unmelted material deposited during the late stages of spraying and are less abundant in the KGa-2 specimen that was subjected to an additional heating cycle (Table 1). The clusters of particles indicate they were transported as aggregates rather than individual particles and there is little sign of any crystallization processes occurring (Figure 5c). In some cases, the glass spheres are coated by platy nanoparticles that are subse-quently covered by fresh patches of glass (Figures 4a and 5d). This indicates they were generated simultaneously with the formation of melt during the plasma spraying process.

Nature of the nanocrystalline particles

The nature of the nanocrystalline particles was revealed by TEM microscopy, EDX and SAED study (Figure 6). Some particles appear as intact KGa-2 kaolinite crystals with clear hexagonal shapes and electron diffraction patterns with some turbostratic rotations that indicate these grains largely escaped dehydrox-ylation (Figure 6a). These types of particles were not abundant and correspond to the small (001) reflection at 0.71 nm observed by XRD study (Figure 3). The more common type of grains are irregular and consist of irregular particles that are welded together to form metakaolinite aggregates. Their electron diffraction patterns indicate strong thermal modifica-tion with no clear periodic crystal pattern and high degrees of disorder attributable to dehydroxylation and decomposition. The loss of structural order appears greater than that of
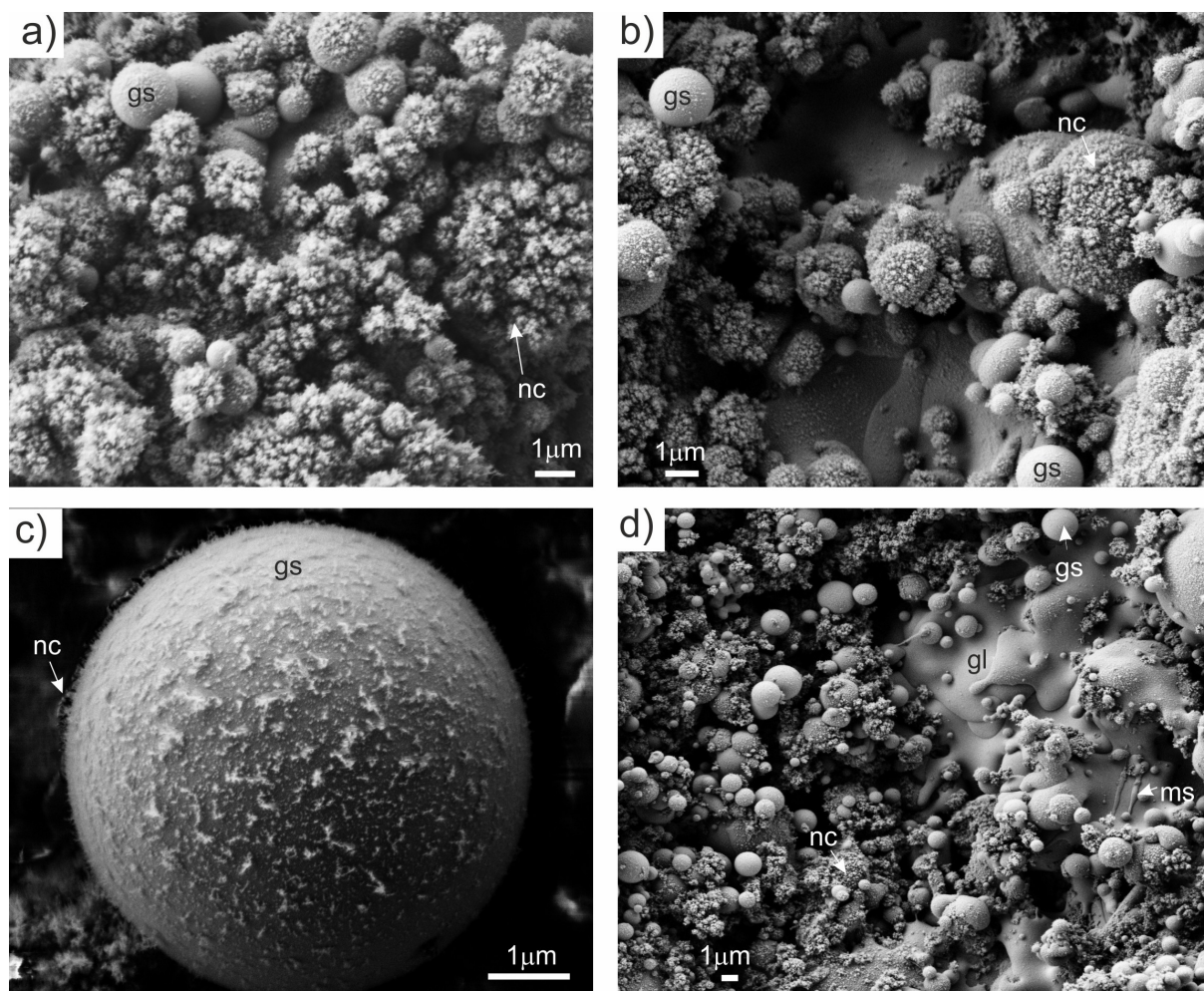
ChemistrySelect

Research Article
doi.org/10.1002/slct.202202820

Chemistry Europe
European Chemical
Societies Publishing

Figure 5. Secondary electron microscope images of unmelted nanocrystalline (nc) particles on the upper surface of the plasma-sprayed glass a) single-layer coating, b) double-layer coating, c) five-layer coating, and d) five-layer coating and additional heat treatment. gs = glass sphere. gl = glass layer. ms = melt striations.

metakaolin documented in the literature, which commonly retains a quasihexagonal periodicity in the (a,b) plane.[47]

EDX analyses of the KGa-2 aggregates (Figure 6c) show compositions similar to the bulk powder composition when adjusted for water content (Table 1). This similarity and the relatively high concentrations of Fe_2O_3 and TiO_2 compared to pure kaolinite compositions indicate that these aggregates include fused kaolinite, anatase, crandallite and mica minerals.

Glass sphere size distributions resulting from plasma melting and quenching

To assess any differences in the plasma coatings between the varieties of kaolinite and the plasma treatments used, the size of the glass spheres was measured from SEM images. Based on ca. 900 measurements per specimen, the dimensions and size distributions indicate that only small variations occur (Table 3 and Figure 7). The average diameters of KGa-1b and KGa-2 prepared under the same conditions of five plasma passes show similar sizes of 1.42 (σ_1 1.28) and 1.33 μm (σ_1 0.98),

respectively. These results indicate that the two kaolinite samples behaved similarly, despite the different states of crystal disordering. There is no clear indication that the defect-poor KGa-1b kaolinite decomposed more rapidly than the less crystalline KGa-2: a feature characteristic in dehydroxylation studies.[34] The slightly larger glass spheres observed in the KGa-1b kaolinite are accompanied by the presence of fewer nanocrystalline particles and indicate more effective melting of the material. As both powders have similar grain sizes (between 650 nm–50 μm), these small differences more likely reflect the behavior of the powder in the plasma beam rather than crystallographic differences in the kaolinite. The lower specific surface area (N_2 area of ca. 10 m^2/g) and smoother surfaces of the KGa-1b particles are suggested to present lower frictional resistance to flow than the KGa-2 powder with a more irregular and higher specific surface area (N_2 area of ca. 24 m^2/g).

The varying number of plasma coatings prepared resulted in comparable glass sphere sizes and size distributions (Figure 6). Five layers produced slightly larger average sizes (1.32 μm, σ_1 1.08) than a single-layered coating (1.14 μm, σ_1

ChemistrySelect

Research Article
doi.org/10.1002/slct.202202820

Chemistry Europe
European Chemical
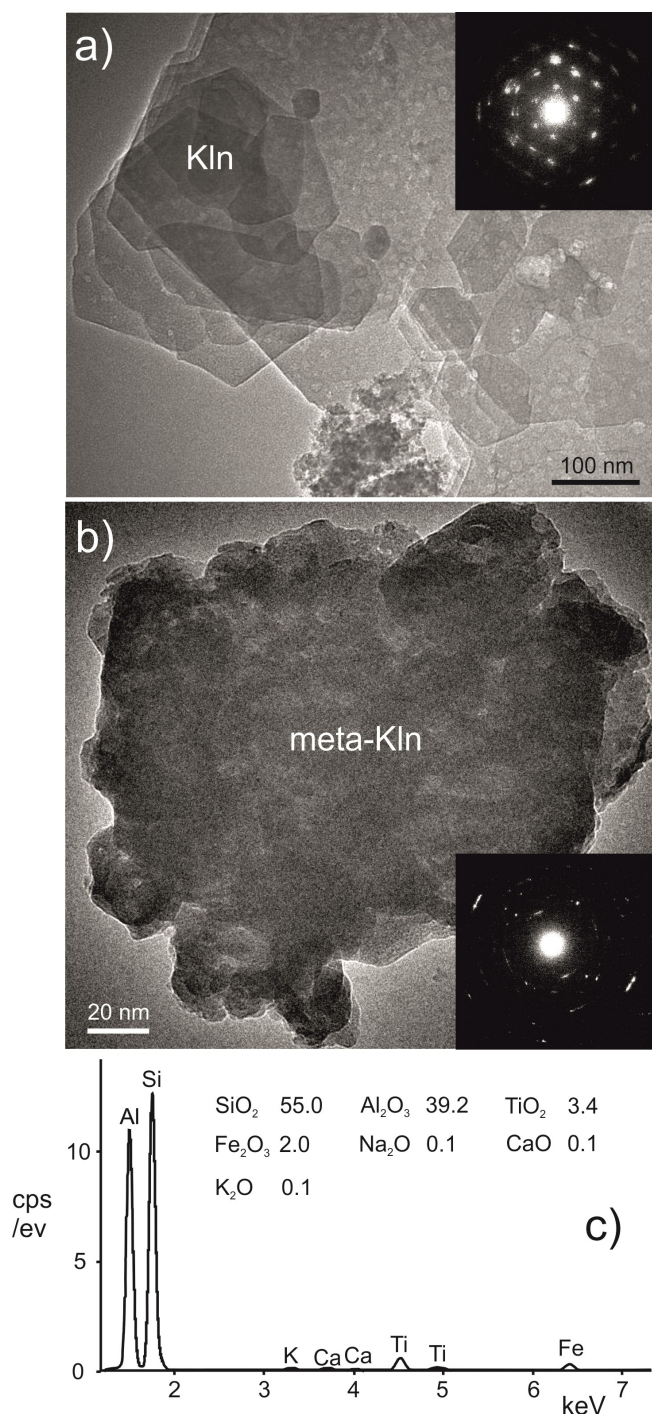Societies Publishing

Figure 6. Transmission electron microscope images and selective area electron diffraction patterns) of unmelted plasma-sprayed kaolinite particles found coating the glass spheres, a) thermally unmodified particles (small speckles represents damage caused by the electron beam), b) dehydroxylated aggregate. C) Energy dispersive analysis of the dehydroxylated and fused aggregate shown in b).
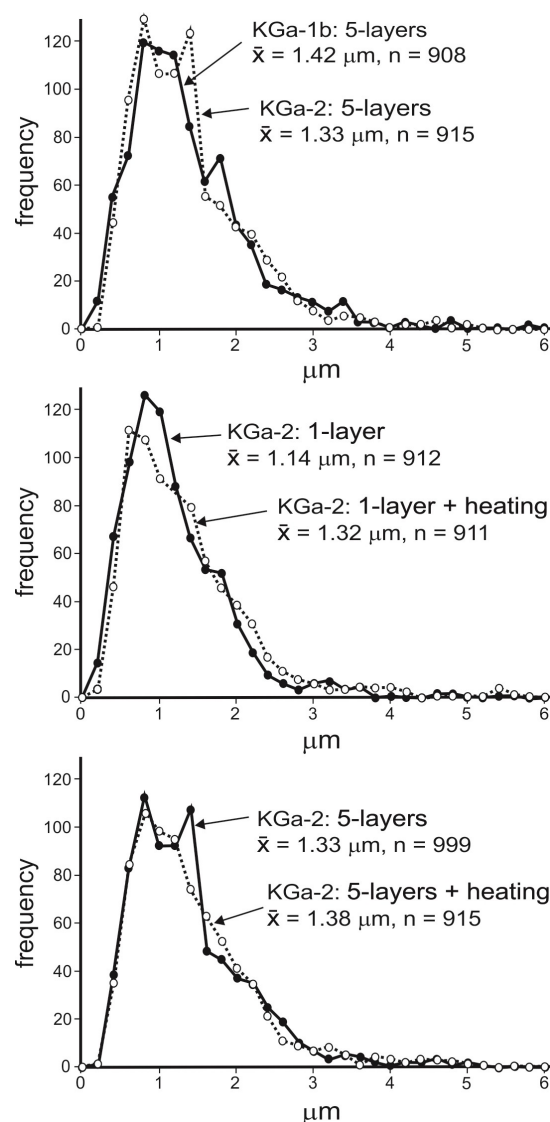

Figure 7. Size distributions of alumino-silicate glass balls in the plasma-coated material.

static heating of the specimens could lead to the development of slightly larger melt spheres, probably as a result of higher plasma and substrate temperatures, as reported by Mostaghimi and Chandra.[48] However, further experimentation is required to confirm that such differences are reproducible. The fact that the glass droplets in most cases produced spheres or deformed spheres indicates that the droplets were either solid or semi-solid at the point of impact. The low abundance of molten splays and striations points to rapid quenching and solidification of viscous droplets at the point of contact with the metal substrate.

FTIR spectroscopy

ATR FT-IR spectroscopy provided information on the typical absorption bands of kaolinite and alumino-silicate glass (Figure 8). In the FT-IR spectra of the powders KGa-1b and KGa-2,

0.92) and an additional stage of static heating also yielded slightly larger glass spheres (1.32 μm σ_1 0.98 for one layer and 1.38 μm σ_1 1.12 for five layers). These small but consistent differences may indicate that multiple plasma treatments or

ChemistrySelect

Research Article
doi.org/10.1002/slct.202202820

Chemistry
Europe
European Chemical
Societies Publishing

Table 3. Glass sphere (Gs) sizes (diameters) for the different plasma treatments. Nc = nanocrystalline particles, Ms = melt striations, AH = additional heating.

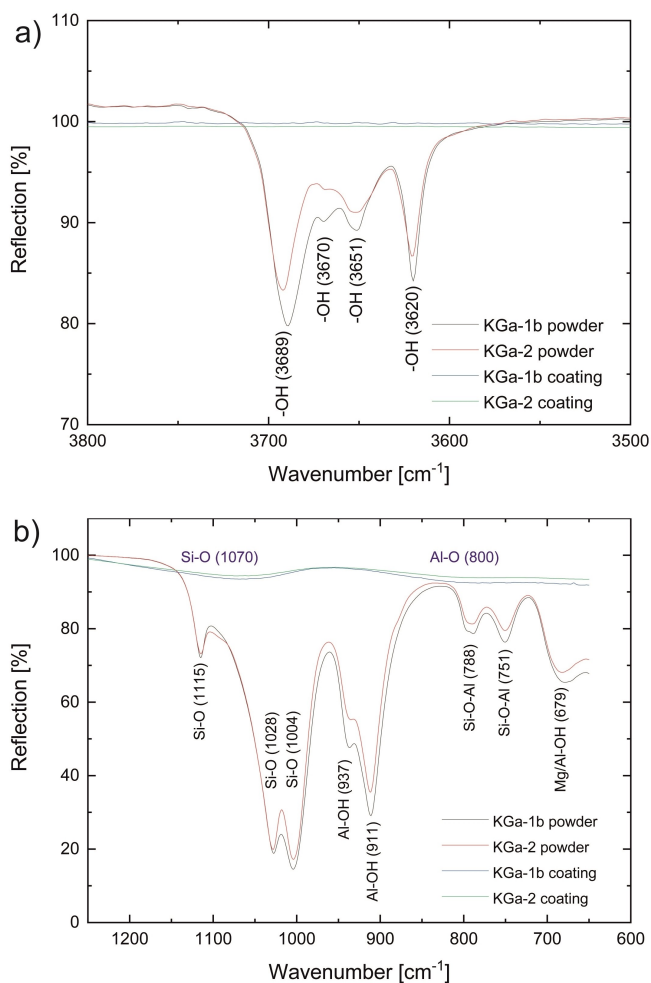| Plasma treatment	n	Average (μm)	Standard deviation (σ_1)	Medien (μm)	Maximum (μm)	Observations
KGa-1b						
5 layers	908	1.42	1.28	1.13	19.2	Gs, less Nc
KGa-2						
5 layers	912	1.14	0.92	0.84	13.9	Gs and Nc
Single-layer + AH	911	1.32	1.08	1.07	10.5	Gs and Nc
Five layers	999	1.33	0.98	1.11	11.6	Gs and Nc
Five layers + AH	915	1.38	1.12	1.14	16.5	Gs, Ms and Nc

Figure 8. FT-IR spectra of kaolinite powders KGa-1b and KGa-2 and atmospheric plasma sprayed coatings. a) Wavenumber range between 3500 to 3800 cm^{-1} and b) wavenumber range between 600 and 1250 cm^{-1}. Absorption lines are labeled after.[50,51]

the characteristic absorption bands of kaolinite could be identified. The absorption bands corresponding to the stretching frequencies of the OH^{-} groups are found at the wavenumbers 3689 cm^{-1}, 3670 cm^{-1}, 3651 cm^{-1}, and 3620 cm^{-1}.[49] Furthermore, in the FT-IR spectra in the range between 500 and 1150 cm^{-1} wavenumbers, various Si–O absorption bands can be detected (1115 cm^{-1} Si–O, 1028 cm^{-1} Si–O, 1004 cm^{-1}

Si–O, 788 cm^{-1} Si–O–Al, 751 cm^{-1} Si–O–Al) as well as some OH^{-} bands, which are in combination with Al bands (679 cm^{-1} MG/Al–OH, 911 cm^{-1} Al–OH, 937 cm^{-1} Al–OH).

In the spectra of the plasma sprayed coatings (Figure 8a), the characteristic bands for kaolinite disappear. All OH^{-} absorption bands in the range between 3750 and 3500 cm^{-1} and the range between 600 and 1250 cm^{-1} are no longer visible, indicating complete dehydroxylation of the material. The characteristic Si–O bands of kaolinite present in the raw clay at 1115, 1028, and 1004 cm^{-1} transform into a single broader absorption band around 1070 cm^{-1} characteristic of the amorphous silica (Figure 8b). Similarly, the Al–O–Si bands at 788 and 751 cm^{-1} transform into a single broad absorption band around 800 cm^{-1}, which is representative of the amorphous phase leaving only weak areas of absorption at 1070 and 800 cm^{-1}, corresponding to Si–O and Al–O, respectively.[50] These weak bands are less prominent than calcined kaolinite where a more distinct band occurs at 1090 cm^{-1} after treatment at 800 °C.[51] This pattern is considered to represent that of a pure, anhydrous, alumino-silicate glass phase.

Hardness and specific surface area

All plasma-spraying tests produced hard and homogenous coatings. When placed in an ultrasonic bath and treated in water at 30 Hz, the small number of fine nanoparticles could be easily removed to leave behind the highly porous substrate that could not be scratched with a stainless steel knife (hardness > 1.8 GPa). Attempts at measuring the hardness using a micro-indentor were not successful due to the uneven surface of the coating. However, the plasma magmavication treatment of Georgian kaolin is known to result in extremely strong vitrified materials with shear strengths > 10 GPa.[52] Therefore the true hardness of the alumino-silicate glass coating is likely to be considerably harder than 1.8 GPa.

Based on the micron-sized alumino-silicate glass balls, a potentially large reactive surface area is considered likely. Assuming an average sphere size of 1 μm and a density estimate of 1.6 g/cm^3 for alumino-silicate glass, a minimum surface area value of 3.8×10^5 cm^2/g (3.8 m^2/g) can be calculated from the following expression (Equation 1):

$$\text{Specific surface area (SSA)} = (6\,W/PD) \times 10^2 \text{ cm}^2 \qquad (1)$$

Where W = weight material (g), P = density (g/cm^3) and D = diameter in μm.

The SSA value of ca. 3.8 m^2/g is notably low compared to nanoporous materials such as activated carbon,[53] silica nano-particle coatings[54] or nano-sized zeolite crystals.[55] However, as the plasma-sprayed glass spheres have a closed internal mesoporosity that is not considered in this calculation, it is likely that the SSA will significantly increase as internal pores become connected during any dissolution and precipitation reactions when chemically activated. Although the reactivity of the coatings was not quantified experimentally in this study, the metastable nature of the alumino-silicate glass is known to be highly unstable in alkali solutions[56] and high rates of reaction are likely to be maintained as internal pores become connected.

Conclusions

1. Plasma spraying of pure kaolin powders can be used to prepare stable, hard and potentially highly reactive porous metastable alumino-silicate glass coatings without the crystallization of high-temperature phases (e.g. spinel, mullite, or cristobalite).

2. The melting process produces glass spheres the size of which is largely independent of the initial defect structures in the kaolinite crystals. Small differences arise due to the flow properties of the powder used. Kaolinite with low specific surface areas and well-defined crystal shapes presumably pose less frictional resistance during flow than more disordered kaolinite with higher specific areas.

3. Small but consistent increases (4–13%) in the average size of glass spheres occurred with the increased number of plasma coating and additional static heating but these minor differences are unlikely to be of significance. There was also a slight reduction in the small amounts of unmelted kaolinite and metakaolinite nanoparticles coating the upper surface of all specimens when preparing multiple layers and by static heating. These unmelted nanoparticles could be easily removed by ultrasonic treatment in a water bath.

4. The glass spheres present in plasma-sprayed coatings are highly porous (ca. 40% largely unconnected pores) and have an estimated specific surface area of ca. 3.8 m^2/g. This value is, however, expected to dynamically increase during dissolution and chemical activation as the internal meso-pores become connected. These properties are ideal for conducting subsequent chemical reactions to further modify surface properties.

Copyright

No copyright issue for figures.

Conflict of Interest

The authors declare no conflict of interest.

Data Availability Statement

The data that support the findings of this study are available from the corresponding author upon reasonable request.

[1] P. Fattahi, G. Yang, G. Kim, M. R. Abidian, *Adv. Mater.* **2014**, *26*, 1846–1885.
[2] E. Goiri, P. Borghetti, A. El-Sayed, E. Ortega, D. G. de Oteyza, *Adv. Mater.* **2015**, *28*, 1340–1368.
[3] G. Zhao, X. Li, M. Huang, Z. Zhen, Y. Zhong, Q. Chen, X. Zhao, Y. He, R. Hu, T. Yang, R. Zhang, C. Li, J. Kong, J. B. Xu, S. Rodney, R. S. Ruoff, H. Zhu, *Chem. Soc. Rev.* **2017**, *46*, 4417–4449.
[4] B. Biswas, L. N. Warr, E. F. Hilder, N. Goswami, M. R. Rahman, J. G. Churchman, K. Vasilev, G. Pan, R. Naidu, *Chem. Soc. Rev.* **2019**, *48*, 3740–3770.
[5] A. F.-M. Guimarães, V. Sampaio, T. Ciminelli, *App. Clay Sci.* **2009**, *42*, 410–414.
[6] Y. Zou, X. Wang, Z. Chen, W. Yao, Y. Ai, Y. Liu, T. Hayat, A. Alsaedi, X. Wang, *Environ. Pollut.* **2016**, *219*, 107–117.
[7] H.-C. Fu, H. You, H.-R. Li, L. N. He, *Front. Chem.* **2019**, *7*, 525.
[8] M. Tului, S. Lionetti, G. Pulci, F. Marra, J. Tirillò, T. Valente, *Surf. Coat. Technol.* **2010**, *205(4)*, 1065–1069.
[9] L. Stoch, I. Waclawska, *J. Therm. Anal. Calorim.* **1981**, *20*, 291–304.
[10] S. Sperinck, P. Raiteri, N. Marks, K. Wright, *J. Mater. Chem.* **2011**, *21*, 2118–2125.
[11] M. F. Al-Hilli, K. T. Al-Rasoul, *Ceram. Int.* **2013**, *39*, 5855–5862.
[12] Q. Wan, F. Raio, S. Shaoxian, R. E. García, R. M. Estrella, C. L. Patiño, Y. Zhang, *Cem. Concr. Compos.* **2017**, *79*, 45–52.
[13] A. Gualtieri, M. Belloto, G. Artioli, S. M. Clark, *Phys. Chem. Miner.* **1995**, *22*, 215–222.
[14] T. Kováří, P. Belsky, P. Novotny, J. Ríha, J. Savková, R. Medlín, D. Rieger, P. Holba, *Constr. Build. Mater.* **2015**, *80*, 98–104.
[15] D. Bridson, T. W. Davies, D. B. Harrison, *Clays Clay Miner.* **1985**, *33(3)*, 258–260.
[16] H. H. Murray, *Applied Clay Mineralogy, Occurrence, Processing and Application of Kaolin, Bentonite, Palygorskite-Sepiolite and Common Clays*, Elsevier Amsterdam **2007**, p. 180.
[17] B. K. Benazzouz, A. Zaoui, A. B. Belonoshko, *Am. Mineral.* **2013**, *98*, 1881–1885.
[18] P. Fauchais, *J. Phys. D* **2004**, *37*, 86–108.
[19] Y. C. Tsui, C. Doyle, T. W. Clyne, *Biomaterials* **1998**, *19*, 2015–2029.
[20] X. Liu, P. K. Chu, C. Ding, *Mater. Sci. Eng.* **2010**, *470*, 275–302.
[21] S. Sampath, *J. Therm. Spray Technol.* **2010**, *19*, 921–949.
[22] A. Vardelle, C. Moreau, J. Akedo, et al., *J. Therm. Spray Technol.* **2016**, *25*, 1376–1440.
[23] D. Koch, G. Mauer, R. Vaßen, *J. Therm. Spray Technol.* **2017**, *26*, 708–716.

ChemistrySelect

Research Article
doi.org/10.1002/slct.202202820

Chemistry Europe
European Chemical
Societies Publishing

[24] A. Rico, A. Salazar, M. E. Escobar, J. Rodriguez, P. Poza, *Surf. Coat. Technol.* **2018**, *354*, 281–296.

[25] S. P. Jena, S. K. Acharya, H. C. Das, P. P. Patnaik, S. Bajpai, *Sustain. Environ. Res* **2018**, *28*, 72–78.

[26] S. Seifert, E. Litovsky, J. I. Kleiman, R. B. Heimann, *Surf. Coat. Technol.* **2006**, *200*, 3404–3410.

[27] S. Seifert, R. B. Heimann, J. I. Kleiman, *J. Spacecr. Rockets* **2006**, *43*, 439–442.

[28] J. D. Celes, P. W. Mayne, *Transp. Res. Rec.* **2000**, *1714*, 65–74.

[29] B. Nevrla, P. Ctibor, V. Koudelkovab, F. Lukac, K. Neufuss, *Bol. Soc. Esp. Ceram. Vidrio* **2020**, *60*, 274–282.

[30] S. J. Chipera, D. L. Bish, *Clays Clay Miner.* **2001**, *49*, 398–401.

[31] A. R. Mermut, A. F. Cano, *Clays Clay Miner.* **2001**, *49*, 381–386.

[32] H. van Olphen, J. J. Fripiat, *Data Handbook for Clay Materials and Other Non-Metallic Minerals*, Pergamon Press, Oxford **1979**, p. 346.

[33] L. N. Warr, *Mineral. Mag.* **2021**, *85*, 291–320.

[34] B. A. Sakharov, V. A. Drits, D. K. McCarty, G. M. Walker, *Clays Clay Miner.* **2016**, *64*, 314–333.

[35] S. Sperinck, P. Raiteri, N. Marks, K. Wright, *J. Mater. Chem.* **2010**, *21*, 2118–2125.

[36] P. Zemenová, A. Kloužková, M. Kohoutková, R. Král, *J. Therm. Anal. Calorim.* **2014**, *116*, 633–639.

[37] R. E. Grim, *Clay Miner*, McGraw-Hill, New York (2nd Edition) **1968**, p. 596.

[38] A. Gualtieri, M. Belloto, G. Artioli, S. M. Clark, *Phys. Chem. Miner.* **1995**, *22*, 215–222.

[39] S. Guggenheim, A. F. Koster van Groos, *Clays Clay Miner.* **2001**, *49*, 433–443.

[40] I. Dauo, G. L. Lecomte-Nana, N. Tessier-Doyen, C. Peyratout, M. F. Gonon, R. Guinebretiere, *Minerals* **2020**, *10*, 480.

[41] I. Hassan, *Can. Mineral.* **1996**, *34*, 893–900.

[42] J. M. Knaup, J. Marx, T. Frauenheim, *Status Solidi RRL* **2014**, *8*, 549–553.

[43] R. Mishra, R. S. Ningthoujam, *Materials Under Extreme Conditions* (Eds. A. K. Tyagi, S. Banerjee), Elsevier **2017**, 377–410.

[44] T. Shea, B. F. Hougton, L. Gurioli, K. V. Casman, J. E. Hammer, B. Hobden, *J. Volcanol. Geotherm. Res.* **2010**, *190*, 271–289.

[45] B. P. Glass, B. M. Simonson, *Impact Studies*, Springer, Berlin, Heidelberg **2013**, p.716.

[46] S. Kaufhold, A. Reese, W. Schwiebacher, R. Dohrmann, G. Grathoff, L. N. Warr, C. Müller, U. Schwarz-Schampera, K. Ufer, *Springerplus* **2014**, *3*, 598.

[47] F. Bergaya, P. Dion, J.-F. Alcover, C. Clinard, D. Tchoubar, *J. Mater. Sci.* **1996**, *31*, 5069–5075.

[48] J. Mostaghimi, S. Chandra, *Handbook of Thermal Science and Engineering*, (Ed. F. Kulacki), Springer, Cham **2018**, p. 3043.

[49] J. Madejová, *Vib. Spectrosc.* **2003**, *31*, 1–10.

[50] A. G. San Cristóbal, R. Castelló, M. M. Luengo, C. Vizcayno, *Appl. Clay Sci.* **2010**, *49*, 239–246.

[51] A. Tironi, M. Trezza, E. Irassar, A. Scian, *Procedia Mater. Sci* **2010**, *1*, 343–350.

[52] J. D. Celes, P. W. Mayne, *Transp. Res. Rec.* **2000**, *1714*, 65–74.

[53] Z. Heidarinejad, M. H. Dehghani, M. Heidari G Javedan, M. Sillanpää, *Environ. Chem. Lett.* **2020**, *18*, 393–415.

[54] D. Borisova, H. Möhwald, D. G. Shchukin, *ACS Nano* **2011**, *5(3)*, 1939–1946.

[55] Y. Lv, Z. Qian, B. Tu, D. Zhao, *Catal. Today* **2013**, *204*, 2–7.

[56] C. Panagiotopoulou, E. Kontori, T. Perraki, G. Kakali, *J. Mater. Sci.* **2007**, *42*, 2967–2973.